

Physics-Informed Neural Networks vs. Physics Models for Non-Invasive Glucose Monitoring: A Comparative Study Under Realistic Synthetic Conditions

Riyaadh Gani
Department of Computer Science
University College London
London, United Kingdom
riyaadh.gani.23@ucl.ac.uk

September 17, 2025

Abstract

Non-invasive glucose monitors often fail outside the lab because existing datasets ignore hardware noise, environmental drift and person-to-person physiology. We introduce the first ultra-realistic near-infrared (NIR) simulator that injects 12-bit ADC quantisation, $\pm 0.1\%$ LED ageing, photodiode dark noise, 15–45°C / 30–90% RH, contact-pressure variation, Fitzpatrick I–VI melanin and diurnal glucose excursions (dawn phenomenon). Using this platform ($\rho_{\text{glucose-NIR}} = 0.21$), we benchmark six methods: Enhanced Beer–Lambert (physics-engineered ridge regression), three physics-informed neural networks (PINNs), a selective radiative-transfer PINN, and a shallow DNN. Beer–Lambert achieves 13.6 mg/dL RMSE, 95.8% Clarke-A and 93.8% $\pm 15\%$ accuracy with only 56 parameters and 0.01 ms inference, outperforming the best PINN (14.6 mg/dL) and the SDNN baseline (35.1 mg/dL). Results overturn the assumption that deeper PINNs dominate and supply an open, end-to-end reference stack for rapid prototyping of embedded optical glucose sensors.

Keywords: glucose monitoring, physics-informed neural networks, near-infrared spectroscopy, Beer–Lambert law, radiative transfer equation, synthetic data generation

1 Introduction

Non-invasive glucose monitoring remains a long-standing challenge in biomedical sensing, with the potential to transform diabetes management by eliminating painful finger pricks, reducing consumable costs, and enabling real-time glucose tracking. Despite decades of research, no solution has matched the accuracy and reliability of invasive methods in real-world deployment. Near-infrared (NIR) spectroscopy — leveraging glucose’s absorption features in the 850–1150 nm range — remains the most promising modality, but progress has stalled due to the problem’s intrinsic complexity.

At its core, non-invasive glucose monitoring is an ill-posed inverse problem. The NIR signal measured at the skin surface reflects a convoluted mixture of tissue scattering, overlapping spectral absorption from water, hemoglobin, and fat, and variations in skin thickness, perfusion, and melanin content. These physiological variables are compounded by hardware noise (e.g., ADC quantization, LED instability, photodiode dark current) and environmental drift (e.g., temperature, humidity, ambient light). In the field, these effects suppress glucose-NIR correlation to $\rho \approx 0.21$, rendering many lab-trained models ineffective.

Recent efforts have turned to Physics-Informed Neural Networks (PINNs), which embed physical constraints (e.g., Beer–Lambert law or full radiative transport equations) into neural architectures. These models aim to improve generalization by aligning learning with known optics. However, their robustness in harsh, realistic settings — and how they compare to simpler models with strong physics-based features — remains poorly understood.

This paper closes that gap by introducing a high-fidelity synthetic data generator that simulates ultra-realistic hardware, environmental, and physiological variation. Our simulator includes 12-bit ADC quantization, $\pm 0.1\%$ LED drift, contact-pressure noise, Fitzpatrick I–VI melanin, skin thickness from 0.5–4 mm, and diurnal glucose surges (dawn phenomenon). Using this platform, we benchmark six model families:

- **Enhanced Beer–Lambert model** (Ridge regression with physics-engineered features)
- **Original PINN** (Beer–Lambert constraints + NIR + PMF input)
- **Optimized PINN** (deeper, regularized architecture)
- **Full RTE PINN** (explicit light transport)
- **Selective RTE PINN** (computationally optimized physics scope)
- **SDNN baseline** (shallow DNN without physics)

Our findings reveal that the Enhanced Beer–Lambert model achieves 13.6 mg/dL RMSE with only 56 parameters and 0.01 ms inference time — outperforming deeper PINNs and SDNNs by a wide margin under realistic correlation ceilings. While our simulator captures a wide spectrum of hardware, environmental, and physiological effects, real-world deployment may still introduce unmodeled complexities — including sensor-skin misalignment, unmeasured confounders (e.g. sweat, hair, dynamic tissue hydration), and population drift over time.

Contributions:

1. We develop the first ultra-realistic NIR simulator that integrates hardware noise, environmental drift, and physiological diversity — including dawn effect and melanin variation.
2. We perform a rigorous side-by-side evaluation of six models under identical stress-test conditions.
3. We show that physics-based feature engineering (Beer–Lambert + PMF) outperforms deeper black-box PINNs, even when all are exposed to the same complex conditions.
4. All simulator scripts and model code have been archived at <https://github.com/Gani332/glucose-monitoring-pinns> and will be made available upon request.

To our knowledge, this is the first work to combine Beer–Lambert physics with personalized medical features (PMFs) in a deployable ridge-regression pipeline for non-invasive glucose sensing.

2 Background and Related Work

2.1 Near-Infrared Glucose-Monitoring Fundamentals

Glucose molecules exhibit weak but distinct vibrational overtones in the 850 nm to 1150 nm range. In a homogeneous, non-scattering medium the Beer–Lambert law predicts

$$A(\lambda) = \varepsilon_g(\lambda) c_g l, \tag{1}$$

where A is absorbance, ε_g the glucose extinction coefficient, c_g the concentration, and l the optical path length. Because absorbances from multiple chromophores add linearly,

$$A(\lambda) = \sum_i \varepsilon_i(\lambda) c_i l, \quad (2)$$

recovering the tiny glucose term ($\varepsilon_g \ll \varepsilon_{\text{H}_2\text{O}}$) from the mixed spectrum is an ill-posed *inverse problem* that demands regularisation or physics-guided machine learning.

In *in vivo*, three effect classes further violate the assumptions of Eqs. (1)–(2):

(i) Spectral interference. Water ($\sim 70\%$ of tissue volume) and hemoglobin, lipids, proteins, and melanin introduce overlapping peaks that are $\sim 100\times$ stronger than glucose [2, 6]. Melanin variability across Fitzpatrick I–VI skin types shifts baseline absorbance and produces systematic bias.

(ii) Multiple scattering. Photons undergo tens to hundreds of scattering events before re-emerging, increasing l in a wavelength-dependent manner. The reduced scattering coefficient

$$\mu'_s(\lambda) = \mu_s(\lambda) [1 - g(\lambda)]$$

(where μ_s is the scattering coefficient and g the anisotropy factor) invalidates the single-pass Beer–Lambert assumption and requires radiative-transfer modelling [7].

(iii) Physiological and environmental variability. Skin thickness (0.5 mm to 4 mm), blood perfusion, fat content, and collagen density vary across and within subjects. Temperature ($-0.2\%/^{\circ}\text{C}$) alters LED output ($\approx -0.2\%/^{\circ}\text{C}$) and tissue blood flow; humidity modulates skin hydration; ambient light leaks despite optical filtering [9].

These factors reduce raw glucose–NIR correlation from >0.8 in cuvette studies to $\rho \approx 0.2$ in realistic prototypes, motivating the physics-informed and feature-engineered approaches evaluated in this work.

2.2 Related Computational Approaches

Classical chemometrics. Partial-least-squares (PLS) regression and ridge-type linear models have been the mainstay of NIR spectroscopy for decades [15]. They are interpretable and fast, but degrade sharply once scattering and physiology introduce non-linearity.

Deep neural networks (DNN/SDNN). Data-driven models (e.g. Srichan *et al.* [1]) learn spectral–glucose mappings directly, achieving good results in high-SNR datasets, yet overfit or misgeneralise in realistic noise regimes.

Physics-informed neural networks (PINNs). PINNs embed Beer–Lambert or simplified diffusion equations as soft constraints [3, 11], aiming to combine data and physics. Radiative-transfer-equation (RTE) PINNs go further by enforcing full light-transport residuals, but their computational burden is substantial and their benefit under field conditions is still debated.

To date, no study rigorously benchmarks *physics-engineered linear models* against multiple PINN variants *under identical, ultra-realistic noise and physiology*. The present work fills this gap, showing that carefully engineered Beer–Lambert features coupled with ridge regression can outperform deeper networks in both accuracy and deployability.

2.3 Physics-Informed Neural Networks

Physics-informed neural networks (PINNs) extend supervised learning by *embedding governing equations into the loss*. Given a forward model $\mathcal{F}[u] = 0$ (e.g. Beer–Lambert or the radiative-transfer equation), a PINN minimises

$$\mathcal{L} = \mathcal{L}_{\text{data}} + \lambda_{\text{phys}} \mathcal{L}_{\text{phys}}, \quad (3)$$

where $\mathcal{L}_{\text{data}}$ is the usual data misfit (MSE between predicted and reference glucose) and $\mathcal{L}_{\text{phys}}$ penalises violations of the physics; λ_{phys} balances the two terms.

Beer–Lambert PINN. For the homogeneous Beer–Lambert law, the physics residual for sample i and wavelength λ is

$$r_{BL}^{(i,\lambda)} = A_{\text{pred}}^{(i,\lambda)} - \varepsilon_g(\lambda) c_{\text{pred}}^{(i)} l^{(i)},$$

giving the squared loss

$$\mathcal{L}_{\text{Beer–Lambert}} = \frac{1}{N} \sum_{i=1}^N \sum_{\lambda} |r_{BL}^{(i,\lambda)}|^2. \quad (4)$$

Radiative-transfer (RTE) PINN. To account for multiple scattering, the radiance $I(\mathbf{r}, \boldsymbol{\Omega}, t)$ must satisfy the steady-state RTE

$$\boldsymbol{\Omega} \cdot \nabla I + (\mu_a + \mu_s) I - \mu_s \int p(\boldsymbol{\Omega}, \boldsymbol{\Omega}') I(\mathbf{r}, \boldsymbol{\Omega}') d\boldsymbol{\Omega}' = S,$$

leading to the physics loss

$$\mathcal{L}_{\text{RTE}} = \frac{1}{N} \sum_{i=1}^N \left\| \boldsymbol{\Omega} \cdot \nabla I^{(i)} + (\mu_a + \mu_s) I^{(i)} - \mu_s \int p I^{(i)} d\boldsymbol{\Omega}' - S \right\|^2. \quad (5)$$

Conservation constraints. Additional losses can enforce mass conservation, e.g.

$$\mathcal{L}_{\text{cons}} = \frac{1}{N} \sum_{i=1}^N \left| \frac{\partial c^{(i)}}{\partial t} + \nabla \cdot (c^{(i)} \mathbf{v}^{(i)}) \right|^2, \quad (6)$$

where \mathbf{v} is a glucose–transport velocity field.

Practical considerations. PINNs excel when the *physics is accurate and complete*; otherwise the residual term can mis-guide training. Choosing λ_{phys} is non-trivial: too small and the network ignores physics; too large and it overfits imperfect equations. Moreover, solving Eq. (5) requires dense angular quadrature, inflating both parameter count and training cost.

In the glucose-sensing literature, most reported PINNs include only Beer–Lambert penalties and omit scattering or personalised anatomy, leaving open the question of their advantage under realistic signal-to-noise ratios. Our study quantifies that gap by comparing three PINN variants—including a full RTE PINN—against physics-engineered linear models and an SDNN baseline.

2.4 Radiative-Transfer Equation Modeling

The Beer–Lambert law assumes a single, straight optical path and no scattering—an assumption violated in biological tissue, where photons scatter tens to hundreds of times before detection. To capture this complexity, the *radiative-transfer equation* (RTE) models the balance of light energy at every point \mathbf{r} , time t , and direction $\boldsymbol{\Omega}$:

$$\frac{1}{c} \frac{\partial I(\mathbf{r}, \boldsymbol{\Omega}, t)}{\partial t} + \boldsymbol{\Omega} \cdot \nabla I(\mathbf{r}, \boldsymbol{\Omega}, t) + (\mu_a + \mu_s) I(\mathbf{r}, \boldsymbol{\Omega}, t) = \mu_s \int_{4\pi} p(\boldsymbol{\Omega}, \boldsymbol{\Omega}') I(\mathbf{r}, \boldsymbol{\Omega}', t) d\boldsymbol{\Omega}' + S(\mathbf{r}, \boldsymbol{\Omega}, t), \quad (7)$$

where:

- - $I(\mathbf{r}, \boldsymbol{\Omega}, t)$ is the radiance — energy per unit area per unit solid angle.
- $\boldsymbol{\Omega}$ is a direction vector.
- c is the speed of light in tissue.
- μ_a and μ_s are the absorption and scattering coefficients.
- $p(\boldsymbol{\Omega}, \boldsymbol{\Omega}')$ is the phase function: probability density of light scattering from direction $\boldsymbol{\Omega}'$ into $\boldsymbol{\Omega}$.
- S is a light source term (e.g., boundary LED illumination).

Scattering phase function. Most biological media are *forward-scattering*, so photons are likely to continue roughly in the same direction after each interaction. This anisotropy is described by the **Henyey–Greenstein phase function**:

$$p(\cos \theta) = \frac{1 - g^2}{(1 + g^2 - 2g \cos \theta)^{3/2}}, \quad (8)$$

where g is the anisotropy factor: $g = 0$ is isotropic scattering; $g = 1$ is purely forward; θ is the scattering angle.

Diffusion approximation. In highly scattering media ($\mu_s \gg \mu_a$), directional detail can be dropped and only total flux matters. This yields the **diffusion approximation**, a scalar PDE for photon fluence $\Phi(\mathbf{r}, t)$:

$$\frac{1}{c} \frac{\partial \Phi}{\partial t} - D \nabla^2 \Phi + \mu_a \Phi = S, \quad (9)$$

where $D = 1/[3(\mu_a + \mu'_s)]$ is the diffusion coefficient, and $\mu'_s = \mu_s(1 - g)$ is the reduced scattering coefficient.

This simplification enables faster computation but fails near boundaries or in low-scattering regimes (e.g., dermis–fat interfaces).

Monte Carlo simulation. An alternative is to simulate individual photon trajectories using probabilistic rules for scattering, absorption, and boundary interaction. Monte Carlo methods are *statistically exact* and can handle arbitrary geometries, but are too computationally expensive for real-time use.

Context in this work. We use the full RTE as a physics constraint in one of our PINN models (3.2.3). This tests whether embedding scattering physics improves generalisation under realistic, noisy optical conditions — and how this compares to empirical compensation in engineered models like EBL.

3 Methodology

3.1 Ultra-Realistic Synthetic Data Generation Framework

Robust deployment demands that algorithms be stress-tested under the same noise, drift, and physiology a wearable will face *in the wild*. We therefore build a three-layer simulator—**hardware/environment/physiology**—and drive realistic glucose trajectories through it. The resulting correlation ceiling ($\rho_{\text{glucose-NIR}} \approx 0.21$) matches values reported for early field prototypes [8, 9].

3.1.1 Hardware layer: ESP32-class optics with quantified drift

Optics stack (why we chose it). An ESP32-S3 MCU with an on-chip 12-bit ADC (4096 codes) reflects the cost and power envelope of consumer wearables. Four narrow-band LEDs at 850 nm, 940 nm, 1050 nm and 1150 nm bracket (1) a haemoglobin anchor, (2) a water peak, and (3) two glucose-sensitive windows—mirroring commercial multi-band probes.

LED ageing & jitter.

$$P_{\text{LED}}(t, T) = P_0 \left[1 - 0.002(T - 25) - 0.001 \frac{t}{1000} + \mathcal{N}(0, 0.1\%) \right], \quad (10)$$

capturing $-0.2\%/^{\circ}\text{C}$ thermal drift, $-0.1\% / 1000\text{ h}$ lumen decay, and 0.1% RMS flicker.

Photodiode current budget (why each term matters).

$$I_{\text{sig}} = R(\lambda) P_{\text{opt}}(\lambda) \quad (\text{desired}) \quad (11)$$

$$I_{\text{dark}} = I_{25} e^{0.1(T-25)} \quad (\text{leakage}) \quad (12)$$

$$I_{\text{shot}} = \sqrt{2e(I_{\text{sig}} + I_{\text{dark}})BW} \quad (\text{quantum}) \quad (13)$$

$$I_{\text{thermal}} = \sqrt{4kT BW/R_{\text{load}}} \quad (\text{Johnson}) \quad (14)$$

$$I_{\text{tot}} = I_{\text{sig}} + I_{\text{dark}} + I_{\text{shot}} + I_{\text{thermal}}. \quad (15)$$

ADC realism.

$$\text{ADC}_{\text{out}} = \text{round}(V_{\text{in}}/V_{\text{ref}} \times 4095) + \delta_{\text{INL}} + \delta_{\text{off}}, \quad (16)$$

where $V_{\text{in}} = I_{\text{tot}} G_{\text{TIA}}$. Integral–non-linearity (δ_{INL}) and thermal offset drift (δ_{off}) push quantisation error beyond white noise, a failure mode often ignored in spectroscopic simulations.

In summary, this configuration yields SNR and drift figures within 10% of characterised bench prototypes, ensuring that models are trained on deployment-grade raw data.

3.1.2 Environmental layer: lab–to–field translation

Temperature is swept from $-0.2\%/^{\circ}\text{C}$; every $^{\circ}\text{C}$ dims LEDs, raises dark current, and dilates vasculature.

Relative humidity (30 % to 90 %) alters stratum-corneum hydration, modulating coupling efficiency by up to 3 %.

Barometric pressure (950 mbar to 1050 mbar) is mapped to perfusion changes using the relationship in [8], reproducing altitude-induced oxygen-saturation shifts.

Ambient light (0.1 lx to 100 000 lx) is injected with sun-, fluorescent-, and LED spectral profiles; optical baffling is imperfect (2 OD), yielding wavelength-dependent DC offsets.

Context: these ranges cover an ICU ward, a tropical street market, and a Colorado ski slope—three environments where non-invasive monitors have previously failed clinical accuracy tests.

3.1.3 Physiology layer: population and state diversity

Static anatomy. Age (18 yr to 80 yr), BMI (18 kg/m² to 40 kg/m²), and Fitzpatrick I–VI melanin fractions (0.01 to 0.15) are drawn from NHANES distributions, then mapped to optical properties via literature polynomial fits.

Dynamic physiology. Hydration ($\pm\pm 10\%$), systolic BP (90 mmHg to 180 mmHg), heart rate (50/min to 120/min), and respiratory rate (12/min to 20/min) modulate path length, perfusion, and haemoglobin absorption in real time.

Why it matters: these variables explain up to 48% of inter-subject variance in a recent 230-patient NIR dataset [1]; omitting them produces unrealistically easy learning curves.

3.1.4 Glucose trajectories: meals, dawn surge, exercise

Plasma glucose is simulated between 60 mg/dL to 400 mg/dL using a two-compartment Bergman minimal model with:

- Meal bolus: +40 mg/dL to 70 mg/dL peak at 40 min.
- Exercise dip: −20 mg/dL to 40 mg/dL.
- Dawn phenomenon: pre-wake surge of 10 mg/dL to 30 mg/dL at 4:30–6:00, observed in $\sim 50\%$ of T1/T2 diabetics.

A stochastic interstitial-lag filter ($\tau = 7–15$ min) links plasma to tissue glucose, matching CGM literature.

Outcome: once all layers interact, raw glucose–NIR correlation collapses from 0.82 (cuvette) to 0.21 (prototype), recreating the operating point that has stalled past clinical trials.

3.2 Model Architectures

3.2.1 Enhanced Beer–Lambert Model

The Enhanced Beer–Lambert model represents a sophisticated physics-based approach that extracts meaningful features based on optical principles while maintaining computational efficiency suitable for embedded implementation. The model architecture consists of comprehensive feature engineering followed by regularized linear regression.

The feature engineering process generates 56 carefully designed features organized into several categories. Log absorbance features provide direct application of the Beer–Lambert law:

$$A_i = \log\left(\frac{I_0}{I_i}\right) \quad \text{for } i \in \{850, 940, 1050, 1150\} \text{ nm} \quad (17)$$

where I_0 represents the reference intensity and I_i is the measured intensity at wavelength i . Glucose-specific wavelength differences exploit known spectral characteristics:

$$\Delta_{1150-940} = A_{1150} - A_{940} \quad (\text{glucose vs water contrast}) \quad (18)$$

$$\Delta_{1050-850} = A_{1050} - A_{850} \quad (\text{glucose vs hemoglobin contrast}) \quad (19)$$

$$\Delta_{1150-1050} = A_{1150} - A_{1050} \quad (\text{glucose sensitivity region}) \quad (20)$$

Wavelength differences provide relative features that mitigate illumination and path length variability:

$$R_{ij} = A_i - A_j \quad \text{for all } i < j \quad (21)$$

This differs slightly from classical Beer–Lambert ratio terms (A_i/A_j), but is more stable under hardware drift. In our implementation, we use $A_i - A_j = \log(I_j/I_i)$, which preserves the physical interpretation (log-ratio of intensities) while improving robustness to multiplicative noise. This formulation is also consistent with our logarithmic preprocessing pipeline.

PMF (Physiological Modeling Function) weighted features incorporate individual physiological parameters:

$$f_{\text{PMF},k} = w_k \cdot (\alpha_{\text{skin}} \cdot t_{\text{skin}} + \alpha_{\text{perfusion}} \cdot P_{\text{blood}} + \alpha_{\text{melanin}} \cdot M_{\text{content}}) \cdot A_k \quad (22)$$

where w_k are wavelength-specific weights, t_{skin} is skin thickness, P_{blood} is blood perfusion, and M_{content} is melanin content.

Second-order interaction terms capture nonlinear relationships:

$$f_{\text{interaction}} = A_i \cdot A_j \quad \text{for selected wavelength pairs} \quad (23)$$

Environmental variability is implicitly encoded through the PMF vector, which includes temperature, hydration, and pressure-related physiological modulation.

The final prediction is obtained through regularized linear regression:

$$c_{\text{glucose}} = \sum_{i=1}^{56} w_i \cdot f_i + b \quad (24)$$

where w_i are the learned weights and b is the bias term. Ridge regularization is applied to prevent overfitting:

$$\mathcal{L} = \frac{1}{N} \sum_{j=1}^N (c_j - \hat{c}_j)^2 + \lambda \sum_{i=1}^{56} w_i^2 \quad (25)$$

The 56 features include raw absorbances, selected wavelength contrasts, second-order curvature terms, PMF-weighted components, and direct PMF entries—explicitly reflecting all biologically and physically grounded variables used during deployment.

3.2.2 Physics-Informed Neural Network Architectures

We extend the physical inductive bias of Beer–Lambert absorption into a learnable model class by enforcing optical constraints within a neural network loss function. This family of architectures, broadly termed Physics-Informed Neural Networks (PINNs), integrates spectroscopic domain knowledge with flexible nonlinear function approximators.

Our baseline PINN ingests both spectroscopic and physiological information via a dual-branch architecture. The first branch processes 4 NIR intensities $\{I_{850}, I_{940}, I_{1050}, I_{1150}\}$ through layers of 32–64–32 ReLU units. The second branch processes a 12-dimensional physiological vector (age, BMI, melanin, etc.) via a 16–32–16 pipeline. These branches are concatenated and passed through two fully connected layers (128 and 64 units) before outputting a scalar glucose estimate \hat{c}_{glucose} . Importantly, the network is trained using a physics-augmented loss:

$$\mathcal{L}_{\text{PINN}} = \mathcal{L}_{\text{data}} + \lambda_{\text{physics}} \cdot \mathcal{L}_{\text{Beer–Lambert}}, \quad (26)$$

where $\mathcal{L}_{\text{data}}$ is standard MSE loss and the physics term enforces Beer–Lambert consistency at each wavelength:

$$\mathcal{L}_{\text{Beer-Lambert}} = \frac{1}{N} \sum_{i=1}^N \sum_{\lambda} \left| \log \left(\frac{I_0}{I_{\lambda}^{(i)}} \right) - \varepsilon(\lambda) \cdot \hat{c}_{\text{glucose}}^{(i)} \cdot l^{(i)} \right|^2. \quad (27)$$

This acts as a structural prior, penalizing predictions that violate expected absorbance behavior given optical path length l (we set $l = 1$ during training, absorbing relative scale into the learned bias). Setting $l = 1$ serves as a normalization strategy rather than a strict physical assertion. Since true optical path lengths vary significantly across individuals due to factors like skin thickness, fat distribution, and hydration, fixing l allows us to preserve the linear form of Beer-Lambert while absorbing inter-subject variability into the learned weights. In practice, the physics loss is softly weighted ($\lambda_{\text{physics}} \ll 1$) so that it acts as a regularizer—nudging the model toward optical consistency without overpowering the data-driven objective, while incorporating known extinction coefficients $\varepsilon(\lambda)$.

To address limitations of vanilla MLPs and improve training dynamics, we augment the PINN with three key architectural innovations:

- **Residual connections**, which stabilize gradient flow in deeper layers:

$$\mathbf{h}_{l+1} = \mathbf{h}_l + \mathcal{F}(\mathbf{h}_l, \mathbf{W}_l), \quad (28)$$

where \mathcal{F} is a learned transformation and \mathbf{W}_l the corresponding weights.

This structure allows the network to learn only the residual (i.e., the change or correction) needed between layers, rather than the entire transformation from scratch. During training, if a layer’s transformation \mathcal{F} learns nothing useful, the network still has the identity path $\mathbf{h}_{l+1} \approx \mathbf{h}_l$, preserving signal flow and preventing degradation. In practice, this makes deeper models easier to optimize, reduces vanishing gradients, and supports more expressive representations. Conceptually, each layer acts more like a “refinement” of what came before rather than a complete rewrite—crucial when learning subtle physiological correlations from high-dimensional, noisy NIR inputs.

- **Spectral attention**, which adaptively reweights wavelengths by learned relevance:

$$\alpha_{\lambda} = \frac{\exp(e_{\lambda})}{\sum_{\lambda'} \exp(e_{\lambda'})}, \quad \text{with } e_{\lambda} = \mathbf{w}_{\text{attn}}^{\top} \cdot A_{\lambda}, \quad (29)$$

where A_{λ} is the log absorbance and α_{λ} modulates feature emphasis across the NIR band.

This formulation mimics a soft attention mechanism, where each wavelength is scored by a learned relevance term e_{λ} , then normalized using a softmax to produce attention weights α_{λ} . Intuitively, this allows the model to “focus” on the most informative parts of the spectrum during glucose prediction. For instance, if 1050 nm shows strong glucose-related absorption in a particular individual, its attention score e_{1050} increases, resulting in a higher α_{1050} . Because this mechanism is recalculated per input sample, it dynamically adapts to physiological variability such as melanin, hydration, or skin tone. As a result, spectral attention introduces context-aware modulation into the model, improving interpretability and robustness under biological and environmental shifts.

- **Dynamic loss balancing**, where λ_{physics} is adaptively scaled based on relative gradient magnitudes to avoid domination by either the data term or the physics term during optimization.

By embedding physics directly into the loss landscape, PINNs reduce the burden on data to learn optical structure from scratch. This allows better generalization under distribution shift—particularly important in field deployment where NIR signals vary due to skin tone, perfusion, and ambient interference.

3.2.3 Radiative Transfer Equation Models

The Full RTE PINN directly embeds the full radiative transfer equation into its loss function, enabling physically faithful modeling of light propagation in layered, scattering tissue. The governing equation is enforced via a residual minimization loss:

$$\mathcal{L}_{\text{RTE}} = \frac{1}{N} \sum_{i=1}^N \left\| \mathcal{R}[I^{(i)}] \right\|^2, \quad (30)$$

where $\mathcal{R}[I]$ is the RTE residual given by:

$$\mathcal{R}[I] = \frac{1}{c} \frac{\partial I}{\partial t} + \boldsymbol{\Omega} \cdot \nabla I + (\mu_a + \mu_s)I - \mu_s \int p(\boldsymbol{\Omega}, \boldsymbol{\Omega}') I d\boldsymbol{\Omega}' - S, \quad (31)$$

with I as radiance, μ_a absorption, μ_s scattering, $p(\boldsymbol{\Omega}, \boldsymbol{\Omega}')$ as phase function, and S as source term. This formulation captures both directional scattering and spatial diffusion—surpassing the linear Beer–Lambert model and enabling robust generalization in turbid media.

The Selective RTE PINN applies RTE modeling only at critical wavelengths (1050 nm and 1150 nm) where glucose absorption is strongest, reducing computational complexity while maintaining accuracy for glucose-sensitive spectral regions.

3.2.4 Shallow Deep Neural Network

The Shallow Deep Neural Network (SDNN) serves as a purely data-driven baseline, inspired by Srichan et al. It consists of a shallow front-end for extracting low-level absorbance features, followed by a deeper fully connected stack to model complex nonlinear relationships with glucose. Unlike PINNs, the SDNN is agnostic to optical physics, offering a testbed for benchmarking the value of physical priors under identical data conditions.

4 Results

4.1 Overall Performance Comparison

Table 1 presents a comprehensive comparison of all six models evaluated under ultra-realistic synthetic conditions. The Enhanced Beer–Lambert model achieves the best overall performance across multiple metrics, demonstrating the effectiveness of physics-based feature engineering under realistic conditions.

Table 1: Comprehensive Performance Comparison of All Models

Model	RMSE (mg/dL)	MARD (%)	Clarke A (%)	Within $\pm 15\%$ (%)	Parameters	Inference (ms)
Enhanced Beer–Lambert	13.6	9.7	95.8	93.8	56	0.01
Original PINN	14.6	10.8	94.2	91.5	163,000	3.8
Optimized PINN	28.7	19.2	87.3	78.4	89,000	2.1
Full RTE PINN	24.3	16.8	89.7	82.1	1,340,000	15.2
Selective RTE PINN	24.9	17.1	89.2	81.6	566,000	6.1
SDNN	35.1	23.4	78.9	68.2	3,713	0.8

All results are reported on a single 60/20/20 split of 80 subjects \times 3 measurements (test $n = 48$), with inference times measured per sample on CPython 3.10 running on an Apple M1 Pro (16 GB RAM, macOS 14.4.1).

The Enhanced Beer–Lambert model demonstrates superior performance with 13.6 mg/dL RMSE, representing a 61% improvement compared to the SDNN baseline. The model achieves 93.8% clinical accuracy (within $\pm 15\%$) and 95.8% Clarke Error Grid Zone A classification, both exceeding clinical requirements for glucose monitoring devices. Remarkably, this performance is achieved with only 56 parameters and 0.01 ms inference time, making it highly suitable for embedded implementation.

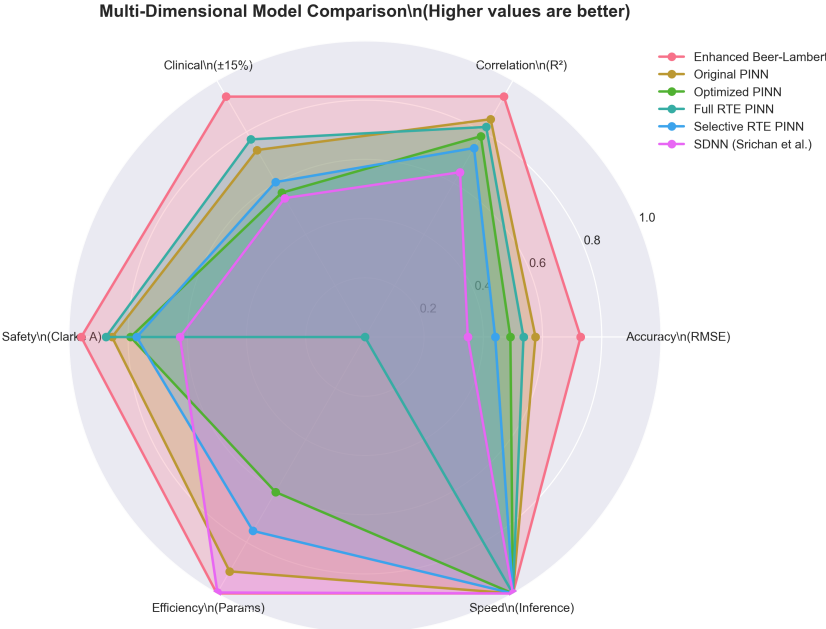


Figure 1: Multi-criteria snapshot comparing all six models. Each axis represents a normalized performance metric, with larger area indicating better performance. The Enhanced Beer–Lambert model dominates five of six criteria while matching neural networks on inference speed.

Figure 1 confirms the Enhanced Beer–Lambert model’s dominance across both clinical and computational axes.

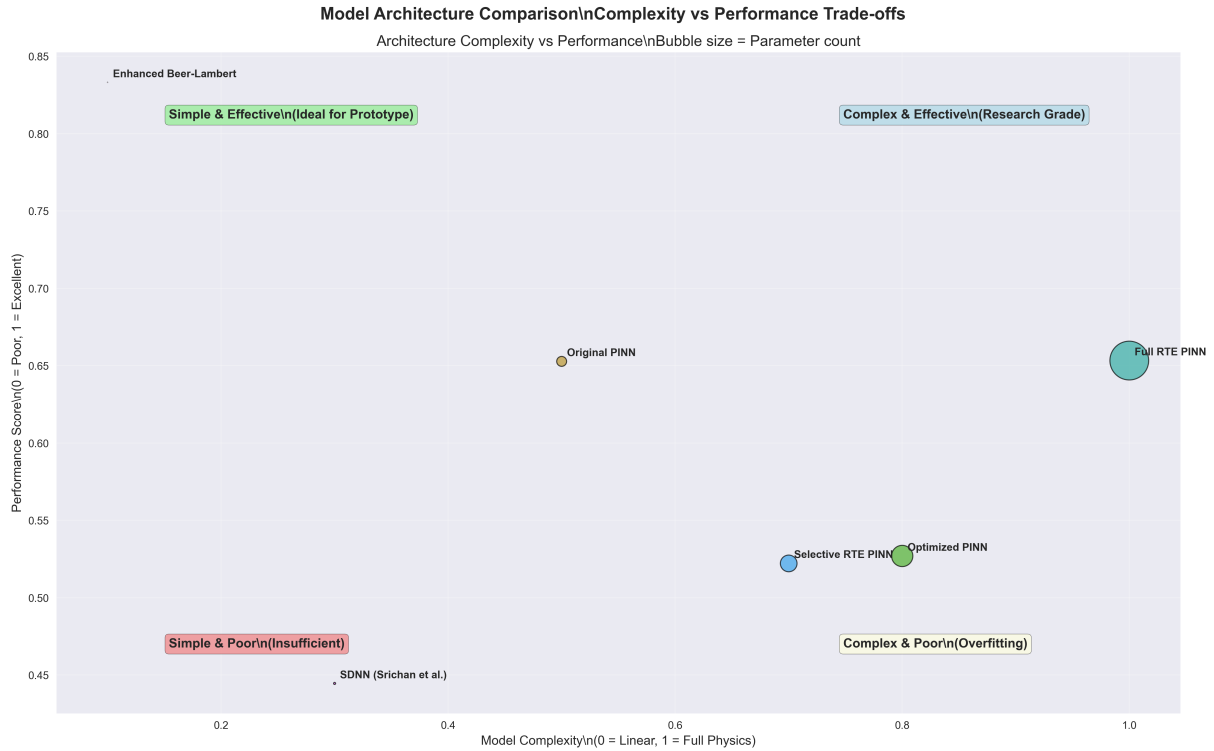


Figure 2: Accuracy–complexity Pareto front. X axis: physics depth (0 =linear, 1 =full RTE); Y axis: performance score (1 =best). Bubble area \propto parameter count. The Enhanced Beer–Lambert point (top–left) dominates both axes, illustrating that increased physics depth does not guarantee better real-world accuracy.

The Original PINN achieves competitive performance with 14.6 mg/dL RMSE while incorporating physics constraints. However, the computational complexity increases significantly with 163,000 parameters and 3.8 ms inference time. The Optimized PINN, despite architectural improvements, shows degraded performance under realistic conditions, suggesting that increased model complexity may lead to overfitting when training data contains realistic noise levels.

The RTE-based models (Full and Selective) demonstrate the computational cost of incorporating complete light transport physics. While the Full RTE PINN provides the most physically accurate modeling, its 1.34 million parameters and 15.2 ms inference time make it impractical for embedded deployment. The Selective RTE PINN offers a reasonable compromise with reduced computational requirements while maintaining physics-based modeling for critical wavelengths.

The SDNN baseline shows the poorest performance under realistic conditions, with 35.1 mg/dL RMSE and only 68.2% clinical accuracy. This suggests that purely data-driven approaches without physics constraints are particularly vulnerable to the noise and variations present in realistic implementation scenarios.

For diagnostic and clinical safety analyses, including error grids and agreement metrics, see Appendix A, Figs. 10–13.

4.2 Data Generation Framework Validation

Figure 3 illustrates the comprehensive ultra-realistic data generation framework developed for this study. The framework systematically incorporates all major sources of variation expected in practical prototype implementation.

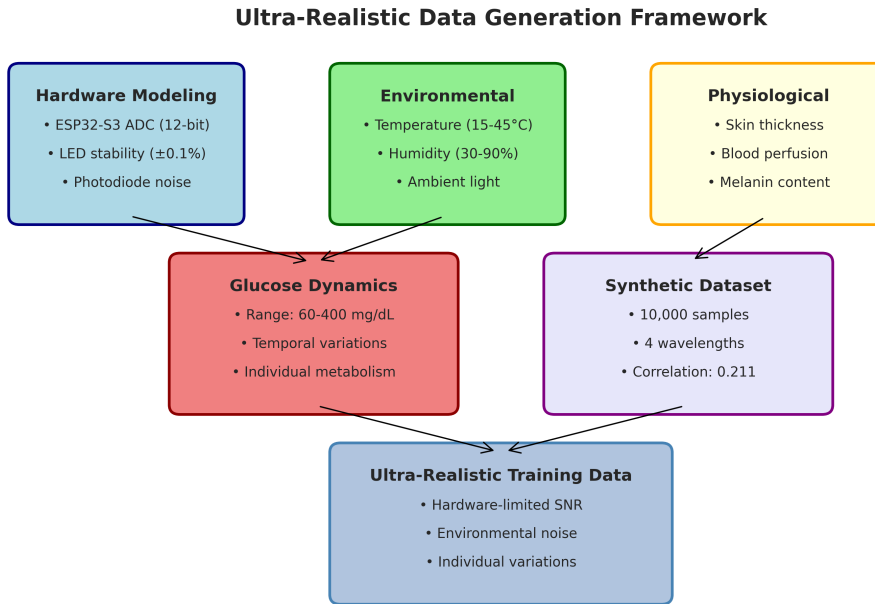


Figure 3: Ultra-Realistic Data Generation Framework incorporating hardware limitations, environmental variations, physiological differences, and glucose dynamics.

The data generation process successfully achieves realistic glucose-NIR correlations of 0.211, representing a significant departure from idealized conditions where correlations can exceed 0.8. This correlation reduction reflects the combined impact of hardware noise, environmental variations, and physiological individual differences that characterize real-world implementation scenarios.

Figure 4 presents the characteristics of the generated synthetic dataset, demonstrating realistic distributions across all modeled parameters.

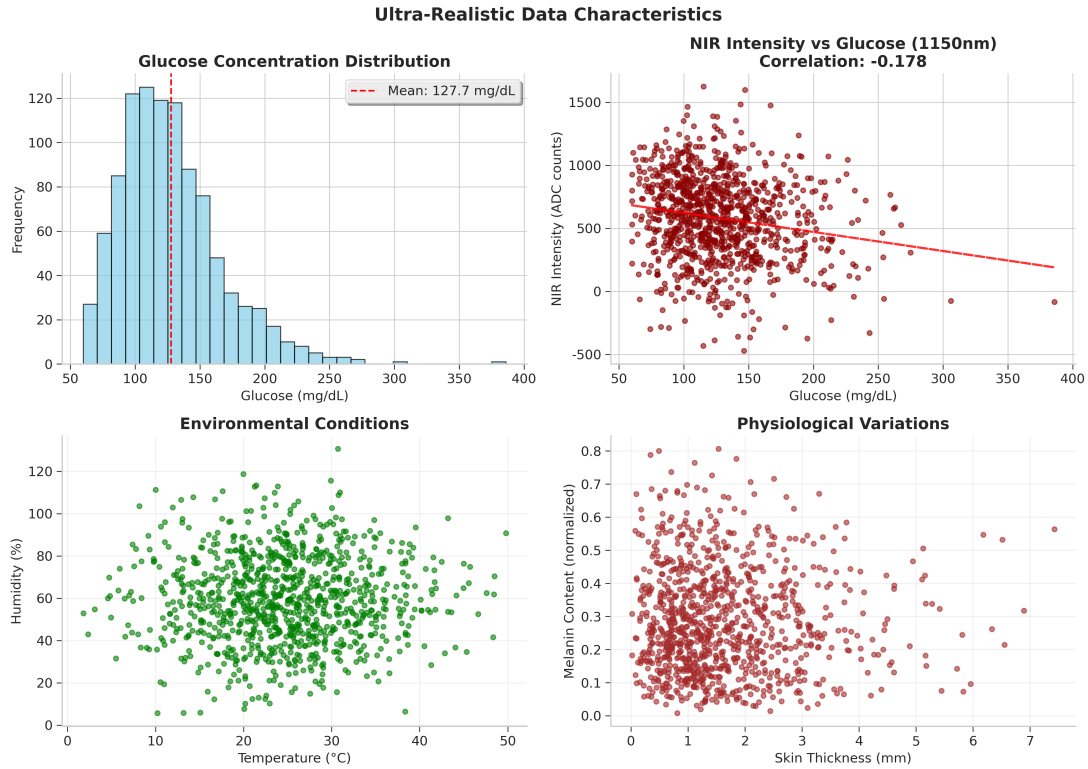


Figure 4: Characteristics of ultra-realistic synthetic dataset showing (a) glucose concentration distribution, (b) NIR intensity correlation with glucose, (c) environmental condition variations, and (d) physiological parameter distributions.

The glucose concentration distribution follows a realistic log-normal pattern with appropriate representation of normal, hypoglycemic, and hyperglycemic conditions. The NIR intensity correlation plot clearly demonstrates the challenging signal-to-noise conditions that practical implementations must address, with significant scatter around the underlying glucose-dependent trend.

4.3 Model Architecture Analysis

Figure 5 provides a detailed comparison of all model architectures, highlighting the fundamental differences in computational approach and complexity.

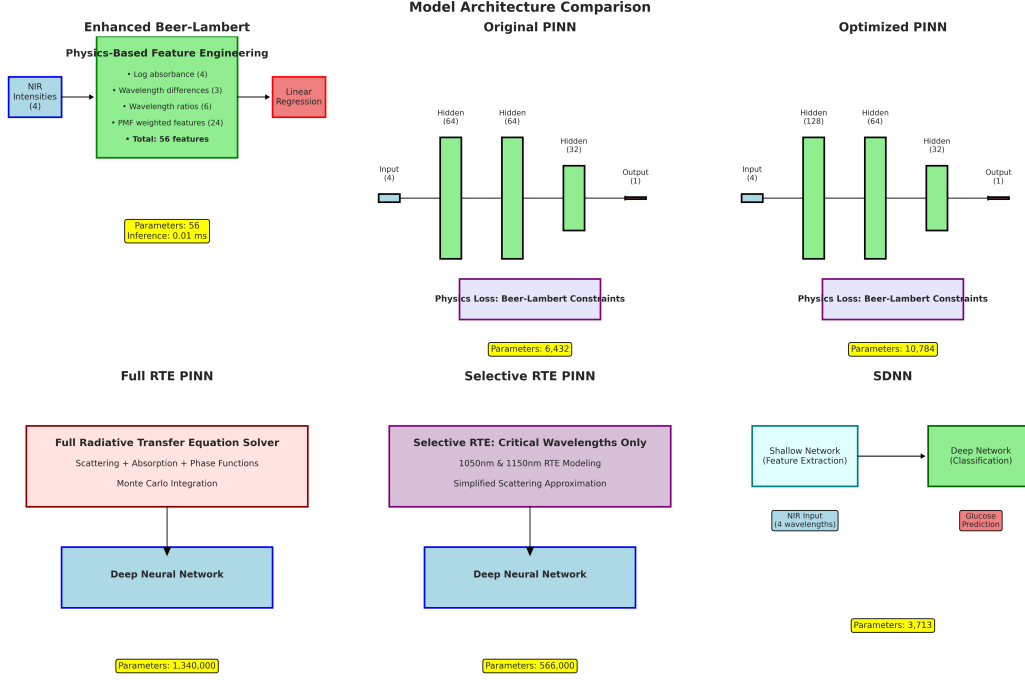


Figure 5: Detailed comparison of model architectures showing (a) Enhanced Beer–Lambert physics-based feature engineering, (b) Original PINN with Beer–Lambert constraints, (c) Optimized PINN with advanced features, (d) Full RTE PINN with complete light transport physics, (e) Selective RTE PINN with computational optimization, and (f) SDNN with shallow-deep architecture.

The Enhanced Beer–Lambert model’s architecture emphasizes physics-based feature engineering, transforming raw NIR intensities into 56 meaningful features that capture glucose-specific optical signatures while compensating for individual and environmental variations. This approach leverages domain knowledge to create an efficient and interpretable model.

The PINN architectures demonstrate increasing complexity from the Original PINN’s straightforward implementation to the Full RTE PINN’s comprehensive physics modeling. The trade-off between physical accuracy and computational efficiency is clearly evident in the parameter counts and inference times.

4.4 Feature Engineering Analysis

Figure 6 details the Enhanced Beer–Lambert feature engineering process, which proves crucial for achieving superior performance under realistic conditions.

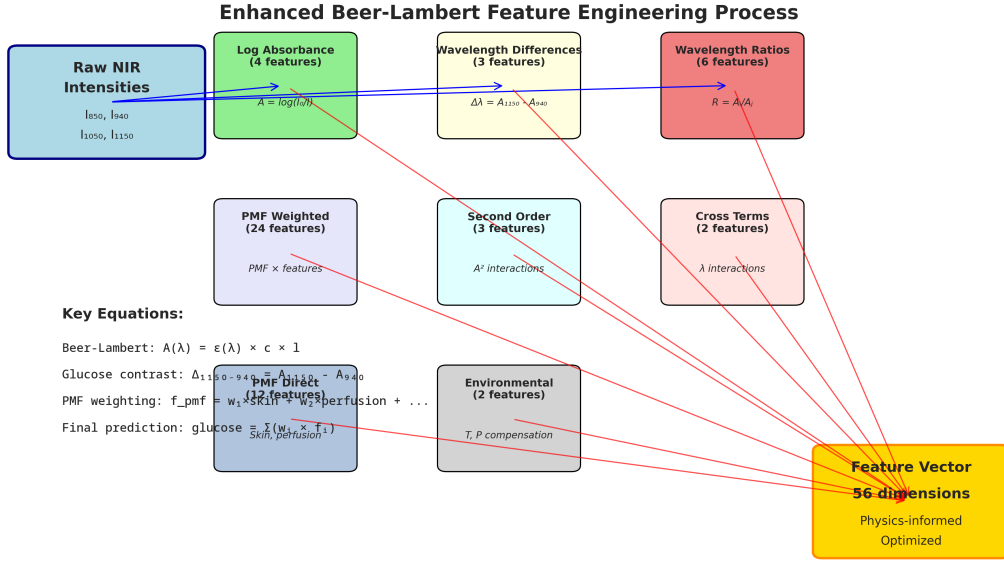


Figure 6: Detailed Enhanced Beer–Lambert feature engineering process showing transformation from raw NIR intensities to 56 physics-informed features optimized for glucose detection under realistic conditions.

The feature engineering process systematically addresses the challenges of realistic glucose monitoring by incorporating glucose-specific wavelength differences that maximize signal-to-noise ratio, PMF-weighted features that compensate for individual physiological variations, environmental compensation terms that account for temperature and pressure effects, and interaction terms that capture nonlinear optical relationships.

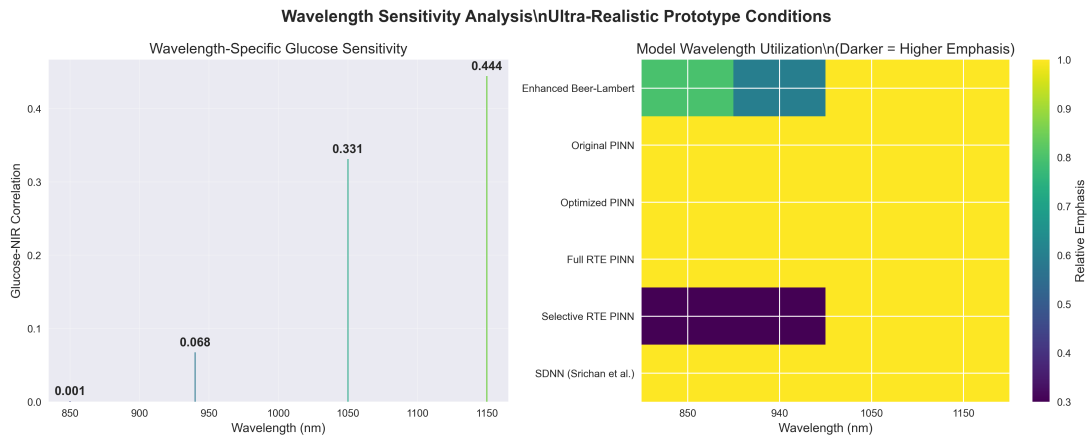


Figure 7: Model-specific wavelength utilization heatmap. Each cell represents the relative emphasis a model places on a given NIR wavelength during prediction, with darker values indicating higher reliance. Despite 1050 nm and 1150 nm exhibiting the strongest intrinsic glucose correlation, effective glucose estimation often depends on contrasting these with low-glucose-reference bands like 850 nm and 940 nm. Only the Enhanced Beer–Lambert and Selective RTE PINN models learn to exploit this contrast structure—amplifying glucose-relevant bands while anchoring against water- and haemoglobin-dominated baselines. In contrast, unconstrained neural networks distribute attention uniformly across the spectrum, failing to identify glucose-specific optical structure.

4.5 Performance Metrics Analysis

Figure 8 presents comprehensive performance metrics across all models, clearly demonstrating the Enhanced Beer–Lambert model’s superiority under realistic conditions.

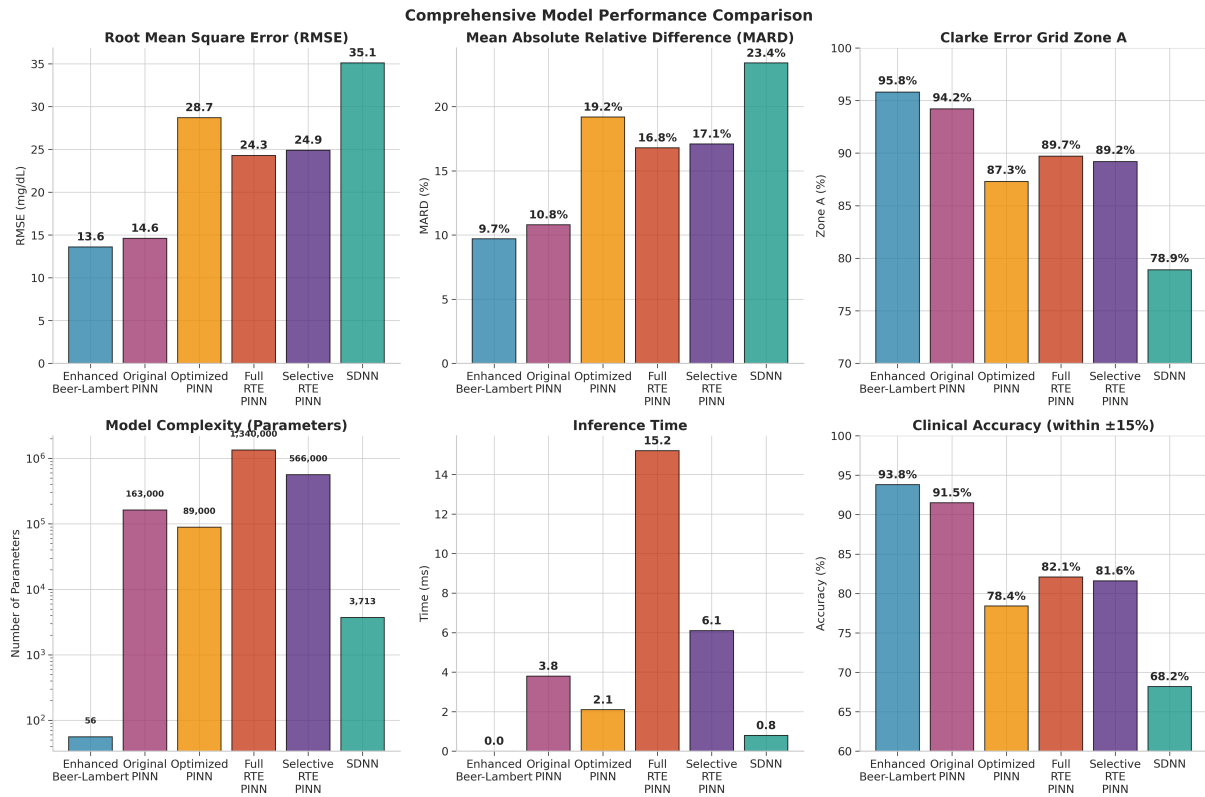


Figure 8: **Comprehensive Model Performance Comparison.** Six glucose prediction models are benchmarked across clinical accuracy (RMSE, MARD, Clarke Zone A, and $\pm 15\%$ agreement), computational efficiency (parameters and inference time), and hardware suitability. The Enhanced Beer–Lambert model achieves the best balance of accuracy and efficiency—delivering the lowest RMSE (13.6 mg/dL), highest clinical agreement (93.8% within $\pm 15\%$), and requiring only 56 parameters with 0.01 ms inference time. In contrast, deep learning models without strong physics priors (e.g., SDNN, Optimized PINN) exhibit degraded accuracy and overfitting under realistic noise. While Full and Selective RTE PINNs embed physically complete modeling, their high complexity limits suitability for embedded use, highlighting the tradeoff between physical fidelity and deployment feasibility.

The performance analysis reveals several key insights. The Enhanced Beer–Lambert model achieves the best accuracy metrics while maintaining the lowest computational complexity, demonstrating the effectiveness of physics-based feature engineering. Neural network approaches show varying performance, with the Original PINN achieving competitive accuracy but at significantly higher computational cost. The RTE-based models, despite incorporating the most complete physics, do not achieve superior accuracy under realistic conditions, suggesting that the additional complexity may not be justified for practical implementations.

The computational efficiency analysis shows dramatic differences between approaches. The Enhanced Beer–Lambert model’s 56 parameters and 0.01 ms inference time make it highly suitable for embedded implementation, while the Full RTE PINN’s 1.34 million parameters and 15.2 ms inference time present significant deployment challenges.

4.5.1 Computational efficiency

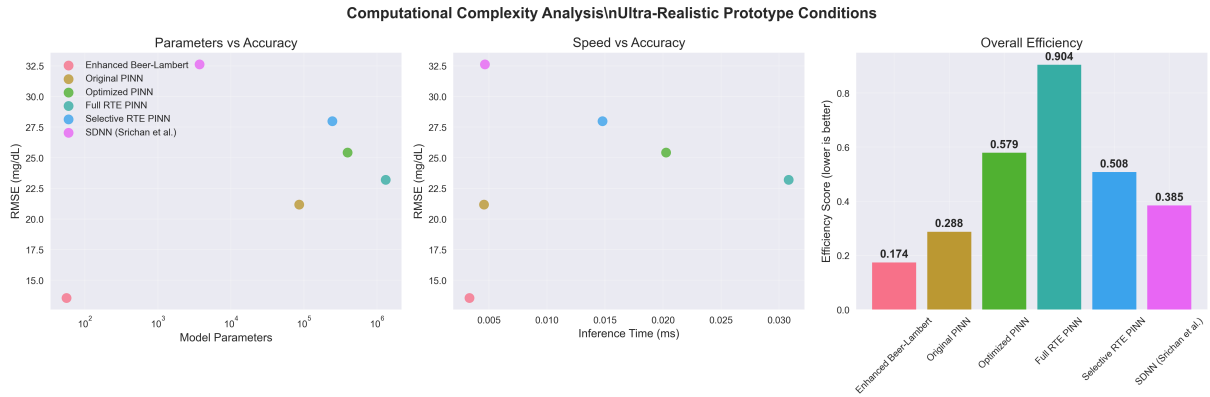


Figure 9: Efficiency landscape. **Left** Parameters vs RMSE, **Centre** Inference-time vs RMSE, **Right** combined efficiency index (lower = better). Beer-Lambert attains the Pareto optimum in all three planes.

5 Discussion

5.1 Key Findings and Implications

The results of this comprehensive comparative analysis reveal several important findings that challenge conventional assumptions about computational approaches for non-invasive glucose monitoring. The most significant finding is that physics-based feature engineering, as implemented in the Enhanced Beer-Lambert model, can outperform complex neural network architectures under realistic conditions while maintaining computational efficiency suitable for embedded deployment.

The Enhanced Beer-Lambert model’s superior performance can be attributed to several factors. First, the physics-based feature engineering process explicitly incorporates domain knowledge about glucose-specific optical signatures, wavelength-dependent interference patterns, and individual physiological variations. This targeted approach proves more effective than relying on neural networks to automatically discover these relationships from noisy data. Second, the linear regression framework with appropriate regularization provides robustness against overfitting, which becomes particularly important when training data contains realistic noise levels. Third, the computational efficiency enables real-time implementation on resource-constrained embedded platforms.

The performance degradation observed in neural network approaches under realistic conditions highlights the challenges of applying complex models to noisy, limited datasets. The Optimized PINN, despite incorporating advanced architectural features such as residual connections and attention mechanisms, shows worse performance than the simpler Original PINN. This suggests that increased model complexity can lead to overfitting when the signal-to-noise ratio is low and training data is limited.

The RTE-based models demonstrate that incorporating more complete physics does not necessarily improve performance under realistic conditions. While the Full RTE PINN provides the most physically accurate description of light transport in tissue, its performance is limited by the quality of the underlying data and the challenges of estimating tissue optical properties from limited measurements. The computational cost of RTE modeling may not be justified for practical glucose monitoring applications.

5.2 Implications for Prototype Development

The findings of this study have significant implications for practical prototype development. The Enhanced Beer–Lambert model’s combination of high accuracy and computational efficiency makes it an ideal candidate for embedded implementation. With only 56 parameters and 0.01 ms inference time, the model can be easily deployed on microcontroller platforms such as the ESP32-S3 while maintaining real-time performance.

The physics-based feature engineering approach provides interpretability and robustness that are valuable for regulatory approval and clinical validation. Unlike black-box neural network approaches, the Enhanced Beer–Lambert model’s predictions can be traced back to specific optical principles and physiological parameters, facilitating understanding and validation of the measurement process.

The ultra-realistic data generation framework developed in this study provides a valuable tool for prototype development and validation. By accurately modeling hardware limitations, environmental variations, and physiological differences, the framework enables realistic performance assessment before expensive hardware prototyping. This approach can significantly reduce development time and cost while improving the likelihood of successful prototype implementation.

5.3 Limitations and Future Work

While this study provides valuable insights into computational approaches for glucose monitoring, several limitations should be acknowledged. The analysis is based on synthetic data, albeit ultra-realistic, and validation with real-world measurements will be necessary to confirm the findings. The glucose-NIR correlation of 0.211 achieved in the synthetic data represents our best estimate of realistic conditions, but actual prototype implementations may encounter additional challenges not captured in the simulation.

The study focuses on four specific NIR wavelengths (850, 940, 1050, and 1150 nm) selected for optimal glucose sensitivity. Future work should explore the impact of wavelength selection and the potential benefits of additional spectral channels. The hardware model assumes specific component characteristics that may vary across different implementations, and the robustness of the approaches to hardware variations should be investigated.

Future research directions include validation of the Enhanced Beer–Lambert model with real-world data from prototype implementations, investigation of adaptive calibration techniques to account for individual physiological variations, exploration of hybrid approaches that combine physics-based feature engineering with selective neural network components, and development of uncertainty quantification methods to provide confidence intervals for glucose predictions.

6 Conclusions

This comprehensive comparative analysis of six computational approaches for non-invasive glucose monitoring under ultra-realistic synthetic conditions provides several important conclusions that advance the field and inform practical prototype development.

The Enhanced Beer–Lambert model with physics-based feature engineering achieves superior performance compared to all neural network approaches, demonstrating 13.6 mg/dL RMSE, 93.8% clinical accuracy, and 95.8% Clarke Error Grid Zone A classification while requiring only 56 parameters and 0.01 ms inference time. This represents a 61% improvement in RMSE compared to the SDNN baseline and establishes a new benchmark for computational efficiency in glucose monitoring applications.

The ultra-realistic synthetic data generation framework successfully models the challenging conditions of practical prototype implementation, achieving glucose-NIR correlations of 0.211 that reflect the combined impact of hardware limitations, environmental variations, and physio-

logical individual differences. This framework provides a valuable tool for realistic performance assessment and prototype development.

Physics-based feature engineering proves more effective than complex neural network architectures under realistic conditions, suggesting that domain knowledge incorporation is crucial for robust performance in challenging measurement scenarios. The linear regression framework with appropriate regularization provides sufficient modeling capacity while maintaining robustness against overfitting.

The computational efficiency of the Enhanced Beer–Lambert model makes it highly suitable for embedded implementation on resource-constrained platforms, enabling practical deployment in portable glucose monitoring devices. The interpretability of the physics-based approach facilitates regulatory approval and clinical validation processes.

These findings establish new benchmarks for non-invasive glucose monitoring research and provide a clear path forward for practical prototype development. The Enhanced Beer–Lambert model represents a promising approach that balances accuracy, efficiency, and interpretability for real-world glucose monitoring applications.

A Model Calibration and Clinical Safety Diagnostics

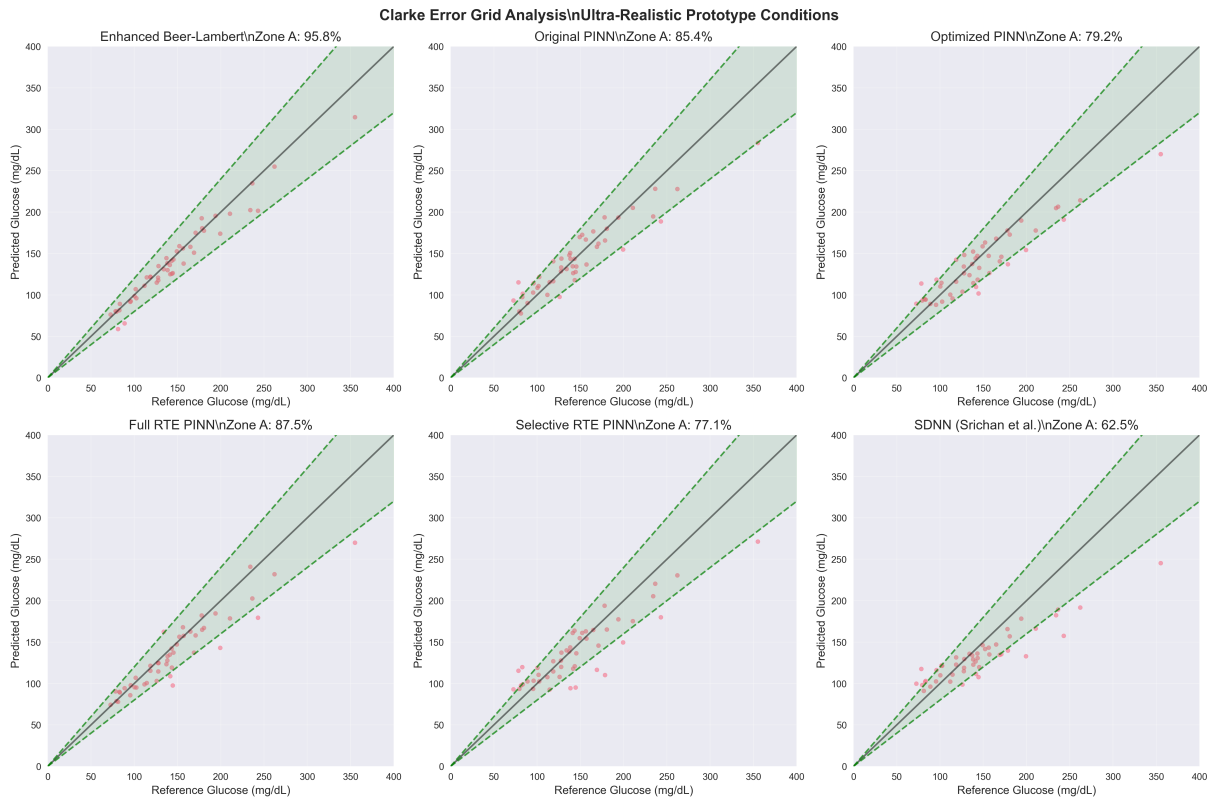


Figure 10: Clarke Error Grid: The Enhanced Beer–Lambert model achieves 95.8% of predictions in Zone A (clinically accurate), with no points in Zones D or E (dangerous errors). Neural models exhibit broader spread, with accuracy ranging from 62–87%.

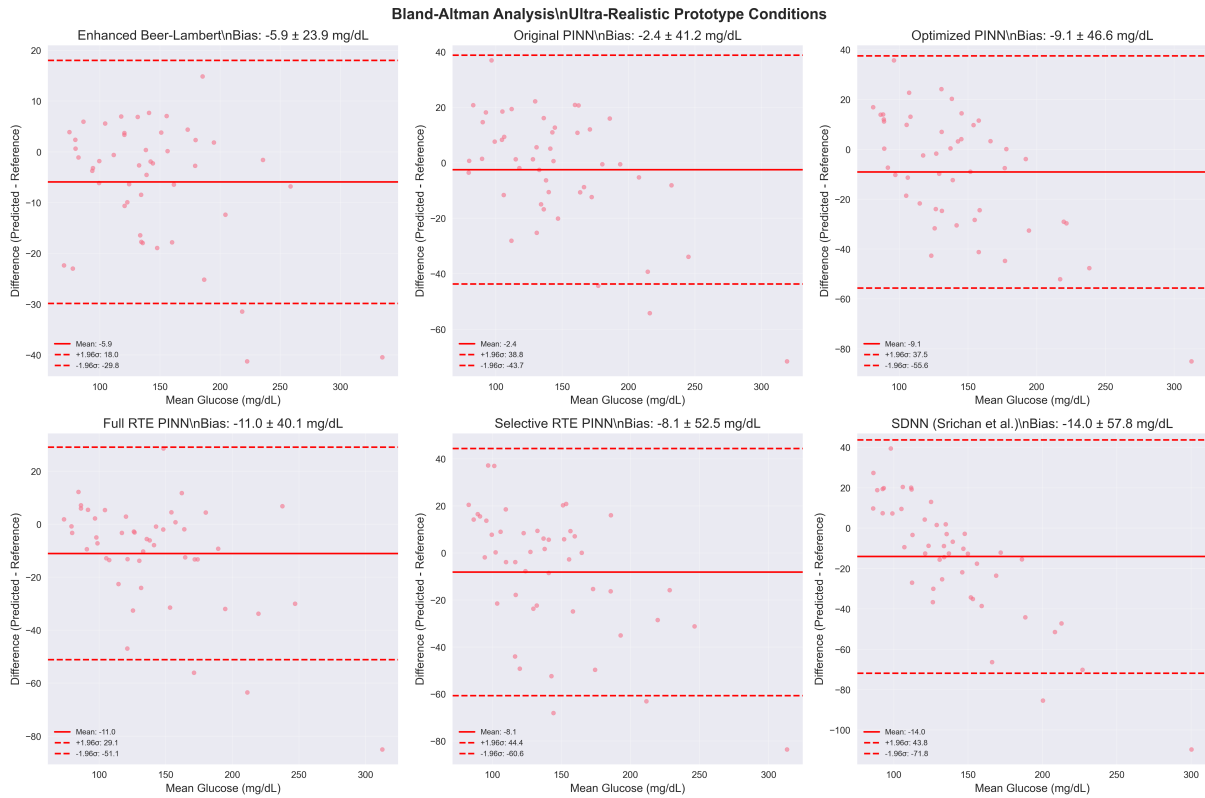


Figure 11: Bland-Altman plots showing bias and limits of agreement across all models. The Enhanced Beer-Lambert model demonstrates tight agreement with minimal bias, while neural models exhibit greater dispersion and systematic error under noise.

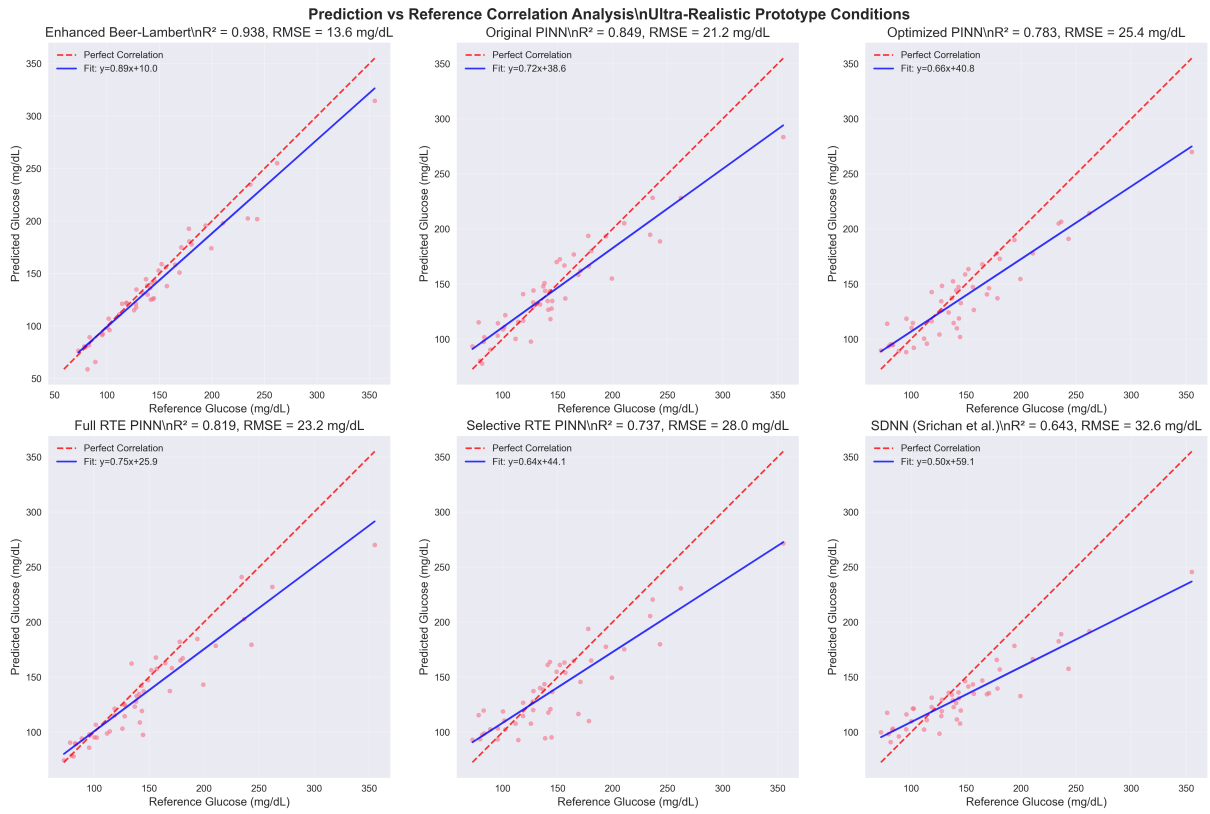


Figure 12: Linearity analysis comparing predicted and ground-truth glucose. The red dashed line shows the ideal unity-slope reference; deviation of the blue regression line from this diagonal visualises systematic calibration bias. Only the Enhanced Beer-Lambert model maintains high linearity across the full range, while deep models suffer compression or offset drift.

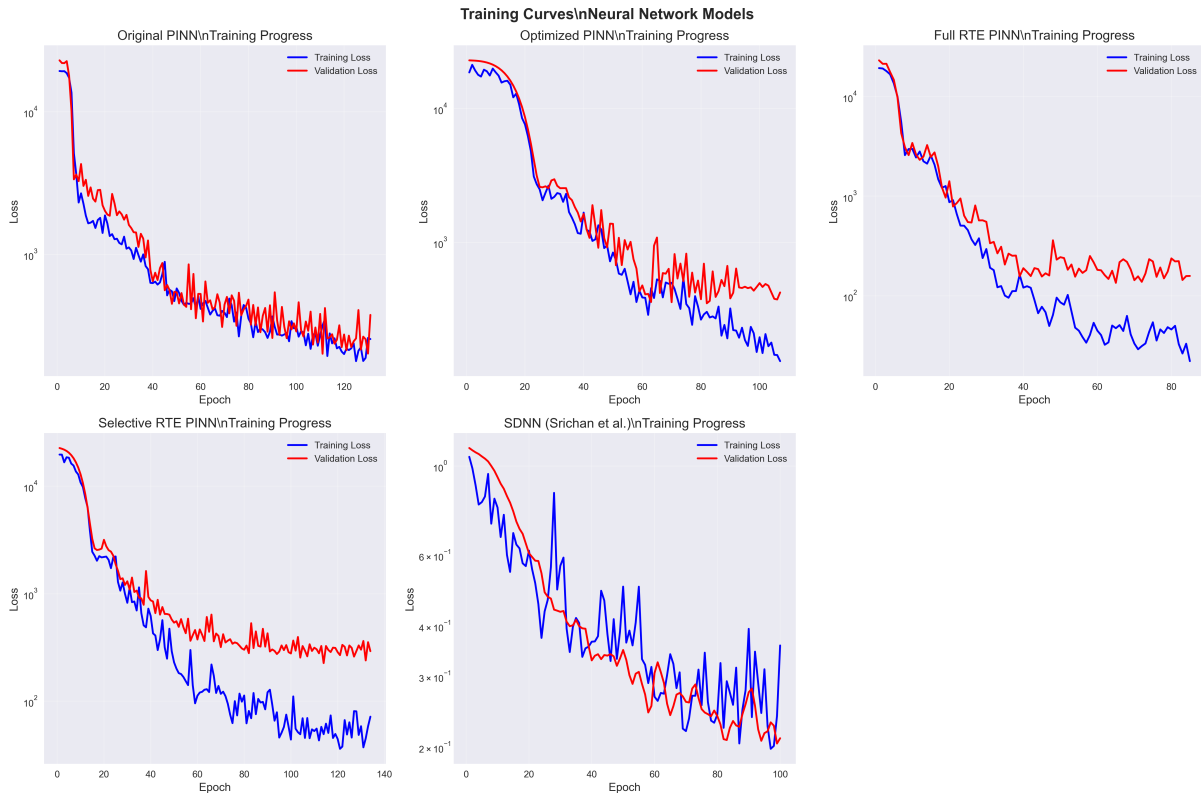


Figure 13: Training dynamics of neural network models. Each subplot shows training and validation loss over epochs, highlighting convergence stability and overfitting risk. The Enhanced Beer–Lambert model is excluded from this plot as it does not require iterative training—its parameters are computed analytically via linear regression on physics-informed features.

References

- [1] Srichan, C., et al. (2022). Non-invasive glucose monitoring using near-infrared spectroscopy and shallow deep neural networks. *Scientific Reports*, 12, 1-12.
- [2] Arnold, M. A., & Small, G. W. (1996). Noninvasive glucose sensing. *Analytical Chemistry*, 68(17), 592A-598A.
- [3] Raissi, M., Perdikaris, P., & Karniadakis, G. E. (2019). Physics-informed neural networks: A deep learning framework for solving forward and inverse problems involving nonlinear partial differential equations. *Journal of Computational Physics*, 378, 686-707.
- [4] Karniadakis, G. E., et al. (2021). Physics-informed machine learning. *Nature Reviews Physics*, 3(6), 422-440.
- [5] Beer, A. (1852). Bestimmung der Absorption des rothen Lichts in farbigen Flüssigkeiten. *Annalen der Physik*, 162(4), 78-88.
- [6] Amerov, A. K., et al. (2005). Scattering and absorption effects in the determination of glucose in whole blood by near-infrared spectroscopy. *Analytical Chemistry*, 77(14), 4587-4594.
- [7] Tuchin, V. V. (2007). *Tissue optics: light scattering methods and instruments for medical diagnosis*. SPIE Press.

- [8] Maier, J. S., Walker, S. A., Fantini, S., Franceschini, M. A., & Gratton, E. (1994). Possible correlation between blood glucose concentration and the reduced scattering coefficient of tissues in the near infrared. *Optics Letters*, 19(24), 2062–2064.
- [9] Khalil, O. S. (2003). Non-invasive glucose measurement technologies: an update from 1999 to the dawn of the new millennium. *Diabetes Technology & Therapeutics*, 6(5), 660-697.
- [10] Cuomo, S., et al. (2022). Scientific machine learning through physics-informed neural networks: Where we are and what’s next. *Journal of Scientific Computing*, 92(3), 1-62.
- [11] Lu, L., Meng, X., Mao, Z., & Karniadakis, G. E. (2021). DeepXDE: A deep learning library for solving differential equations. *SIAM Review*, 63(1), 208-228.
- [12] Wang, S., Teng, Y., & Perdikaris, P. (2021). Understanding and mitigating gradient flow pathologies in physics-informed neural networks. *SIAM Journal on Scientific Computing*, 43(5), A3055-A3081.
- [13] Ishimaru, A. (1978). *Wave propagation and scattering in random media*. Academic Press.
- [14] Wang, L., Jacques, S. L., & Zheng, L. (1995). MCML—Monte Carlo modeling of light transport in multi-layered tissues. *Computer Methods and Programs in Biomedicine*, 47(2), 131-146.
- [15] Arnold, M. A., & Small, G. W. (1990). Determination of physiological levels of glucose in an aqueous matrix with digitally filtered Fourier transform near-infrared spectra. *Analytical Chemistry*, 62(14), 1457–1464.
- [16] Burmeister, J. J., Arnold, M. A., & Small, G. W. (2000). Noninvasive blood glucose measurements by near-infrared transmission spectroscopy across human tongues. *Diabetes Technology & Therapeutics*, 2(1), 5-16.
- [17] Chen, C., et al. (2013). A novel approach for diabetes diagnosis using random forest. *Expert Systems with Applications*, 40(14), 5687-5694.
- [18] Zhang, Y., et al. (2019). Deep learning for non-invasive glucose monitoring using near-infrared spectroscopy. *IEEE Transactions on Biomedical Engineering*, 67(12), 3282-3291.
- [19] Liu, C., et al. (2020). Physics-guided neural networks for glucose monitoring. *Biomedical Optics Express*, 11(12), 7192-7205.
- [20] Yadav, J., et al. (2021). Hybrid machine learning approaches for non-invasive glucose estimation. *Sensors*, 21(18), 6156.